

Article

Mapping the Tilt and Torsion Angles for a 3-SPS-U Parallel Mechanism

Swaminath Venkateswaran ^{1,*}  and Damien Chablat ^{2,†} ¹ Research Center, Léonard de Vinci Pôle Universitaire, La Défense, 92916 Paris, France² École Centrale Nantes, Nantes Université, CNRS, LS2N, UMR 6004, 44000 Nantes, France; damien.chablat@cnrs.fr

* Correspondence: swaminath.venkateswaran@devinci.fr

† These authors contributed equally to this work.

Abstract: This article presents the analysis of a parallel mechanism of type 3-SPS-U. The usual singularity approach is carried out with respect to the Euler angles of the universal joint. However, this approach is computationally expensive especially when stacked structures are analyzed. Thus, the positioning of the mobile platform for the mechanism is analyzed using the theory of Tilt and Torsion (T&T). The singularity-free workspace and the tilt limits of the mechanism are disclosed through this method. These workspaces can then be mapped to the Euler angles of the universal joint and the relation between the T&T space and the Euler space is demonstrated and validated in this study. Initially, simulations are performed using the results of singularity analysis to have a comparison between the T&T space and the Euler space. Experimental validation is then carried out on the prototype of the mechanism to perform a circular trajectory, in line with the simulations. The outcome of this study will be helpful for the integration of the mechanism for a piping inspection robot and also for the analysis of stacked architectures.

Keywords: parallel mechanism; tilt and torsion; singularities; control



Citation: Venkateswaran, S.; Chablat, D. Mapping the Tilt and Torsion Angles for a 3-SPS-U Parallel Mechanism. *Robotics* **2023**, *12*, 50. <https://doi.org/10.3390/robotics12020050>

Academic Editor: Saïd Zeghloul

Received: 16 February 2023

Revised: 20 March 2023

Accepted: 22 March 2023

Published: 24 March 2023



Copyright: © 2023 by the authors. Licensee MDPI, Basel, Switzerland. This article is an open access article distributed under the terms and conditions of the Creative Commons Attribution (CC BY) license (<https://creativecommons.org/licenses/by/4.0/>).

1. Introduction

Parallel kinematics machines (PKM) have interesting applications in industries over serial machines. PKMs offer better accuracy, lower mass/inertia properties and high structural stiffness [1]. The performance of parallel robots varies within their workspace, which is considerably smaller when compared to serial robots. At present, many researchers work on parallel robots as they offer simple and conventional designs with ease of calibration [2]. Moreover, the inverse kinematics, in general, is easier to solve for parallel robots, especially when prismatic joints are employed. With the presence of spherical joints in a parallel mechanism, the modified Euler angles, otherwise known as the “Tilt and Torsion” (T&T) angles, could be employed [3,4]. Bonev et al. [5] proposed the advantages of the T&T angles for the study of spatial parallel mechanisms in-depth. It was demonstrated that there exists a class of parallel mechanisms with zero torsion, which are referred to as zero-torsion parallel mechanisms [5,6]. Another interesting study which exploits the T&T angles is the 3-RRR spherical parallel mechanism, which was analyzed by Tao et al. [7]. This analysis helped in improving the workspace of the parallel mechanism and was applicable for architectures that have revolute joints. Generally, the applications of parallel or spherical mechanisms are found in industrial applications such as machining [8] and nano-alignment, [9]. However, there is another interesting application of a spherical-type parallel mechanism for a piping-inspection robot. A bio-inspired piping-inspection robot that moves like a caterpillar was designed and developed at LS2N, France [10]. This prototype was a rigid model and it was limited to straight pipe profiles. An articulation unit was proposed for this robot which addresses two main issues, namely, passive compliance and active compliance. Passive compliance is applicable for a robot working inside a pipeline having an elbow

at 90° or 45° . In such scenarios, the articulation units usually work in passive modes. Some examples of such mechanisms that exist in the literature are the squirm-type robot of Zhang et al. [11] and the caterpillar-type robot of Kwon et al. [12]. On the other hand, for the active compliance issue, the articulation unit must be actuated in order to align the robot assembly with the pipeline axis or follow a certain direction inside the pipeline. This scenario could be imagined for a robot that passes through a junction or a T-branch inside a pipeline. Some examples of active compliance include the robot of Ryew et al. [13], which employs a dual-actuated universal joint for passing through junctions and a pantograph mechanism to ensure contact with pipeline walls during locomotion. The third criterion that must also be taken into account is the tilt limit of the articulation unit as it determines if the mechanism tilt is sufficient to overcome a bend or a junction. By taking these factors into account, a parallel mechanism that employs three tension springs and a universal joint was incorporated as an articulation unit for a bio-inspired piping inspection robot [10,14]. The positioning of the end-effector with respect to the fixed base plays an important role in identifying the tilt limits of this mechanism. The conventional approach involves analyzing the end-effector for the Euler angles of the universal joint [15]. As the universal joint has two degrees of freedom about the x and y axis, the workspace analysis involves studying the influence of both tilt angles for each position of the end-effector within the joint limits. However, there exists an alternate approach where the end-effector can be localized using the T&T angles. When compared to the Euler space, in the T&T space the singularity analysis appears much simpler as the tilt angle remains constant while the azimuth can vary from 0 to 2π radians or vice versa. This article demonstrates a relation that exists between the T&T space and the Euler space for the 3-SPS-U parallel mechanism under study. This relation, also called the “mapping”, has been demonstrated and validated for the mechanism through simulations and experiments.

The outline of this article is as follows. Section 2 presents the architecture and the geometrical equations of the mechanism using the T&T angles. In Section 3, the singularity analysis of the mechanism is presented in detail through algebraic methods. Following this, in Section 4, the mapping parameters are demonstrated for the T&T space to the Euler space. A numerical simulation is also presented to demonstrate this mapping. Section 5 presents the experimental validation of the mapping theory with the help of the prototype of the mechanism and control laws. Finally, in Section 6, closing discussions are made along with the future perspectives.

2. Architecture of the Parallel Mechanism

This section presents the architecture of the parallel mechanism that will be analyzed in this article. An overview of the final application of this mechanism is first presented. Followed by that, the geometrical equations that are necessary to analyze the singularities are presented.

2.1. A Flexible Mechanism for a Piping Inspection Robot

In collaboration with the enterprise AREVA in France, a rigid bio-inspired piping-inspection robot was designed and developed at LS2N, France. With the help of leg mechanisms and DC motors, the robot accomplishes the locomotion of a caterpillar to move inside a pipeline [10]. A 3D model of this robot and its 2D view are shown in Figure 1. The application of this robot is limited to straight pipelines, as the model is rigid. In order to work inside a pipeline that consists of bends and junctions, a flexible version of the robot was proposed in [14]. Two similar parallel mechanisms with two degrees of freedom (DOF) were introduced between each module of the first robot. These parallel mechanisms consist of a universal joint to constrain the mobility between the base and the mobile platform and three tension springs with or without cables for the actuation. This mechanism can potentially assist the piping-inspection robot to overcome a 90° bend or a junction. A digital model of the flexible piping-inspection robot with the parallel mechanism is shown in Figure 2.

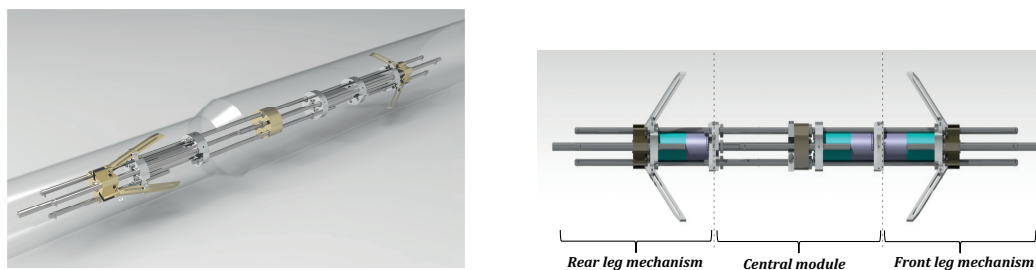


Figure 1. The 3D model (left) and the 2D view (right) of the rigid bio-inspired piping-inspection robot developed at LS2N, France [10].

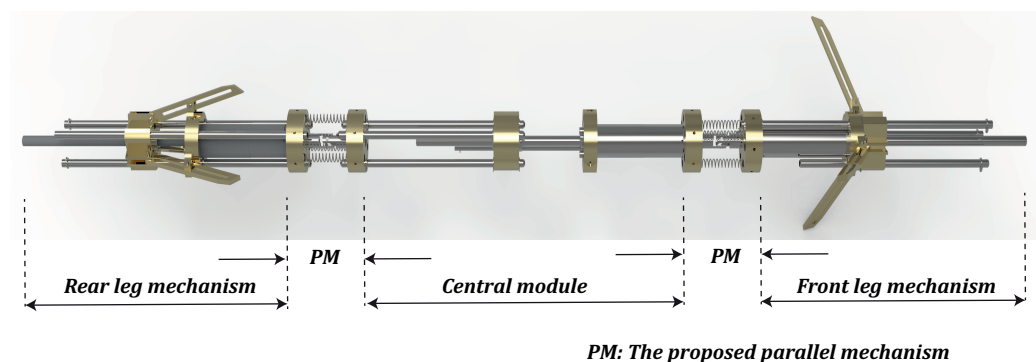


Figure 2. The 2D view of the flexible piping-inspection robot with the parallel mechanism [16].

The primary focus of this article is to analyze the singular configurations of this parallel mechanism which will provide the tilt limits.

2.2. Geometrical Equations of the Mechanism

The parallel mechanism under study was analyzed earlier through two approaches, namely, (i) using the Tilt and Torsion (T&T) angles and (ii) singularity analysis with respect to the Euler angles. The former was employed to study the joint limits where three types of architectures were analyzed to identify an inverse pendulum configuration [17]. On the other hand, the singularity analysis was carried out for the Euler angles, which led to the conclusion that the 3-SPS-U architecture was not an ideal solution for addressing passive compliance owing to the limited tilt angles [15]. In this article, the singularity analysis is revisited for the 3-SPS-U mechanism by using the T&T angles. The articulation unit that consists of the tension springs and universal joints is correlated to a parallel manipulator of type 3-SPS-U [18,19]. The representation of the parallel mechanism under study is shown in Figure 3. In this mechanism, S indicates the spherical joint, U indicates the universal joint and P indicates the actuated prismatic joints or the springs. The mechanism also employs cables that pass through each spring from the base to the end-effector. The cable actuation is performed using external motors in the active modes and it does not resemble a classic prismatic link. Thus, under operation, the mobility of the end-effector is purely obtained through the two rotation angles of the universal joint. The home pose represented in Figure 3a is the position where the tilt angles, as well as the external forces on the mechanism, are equal to zero. The fixed coordinate frame of the base is represented by Σ_0 . The spring mounting points on the fixed base are represented by B_1, B_2 and B_3 and they form an imaginary equilateral triangle of the manipulator base. The vector coordinates for the base mounting points can be written as:

$$\mathbf{b}_i^0 = \begin{bmatrix} r_f \cos\left(\frac{2\pi(i-1)}{3}\right) \\ r_f \sin\left(\frac{2\pi(i-1)}{3}\right) \\ -r_f h \end{bmatrix}, \text{ with } i = 1, 2, 3 \tag{1}$$

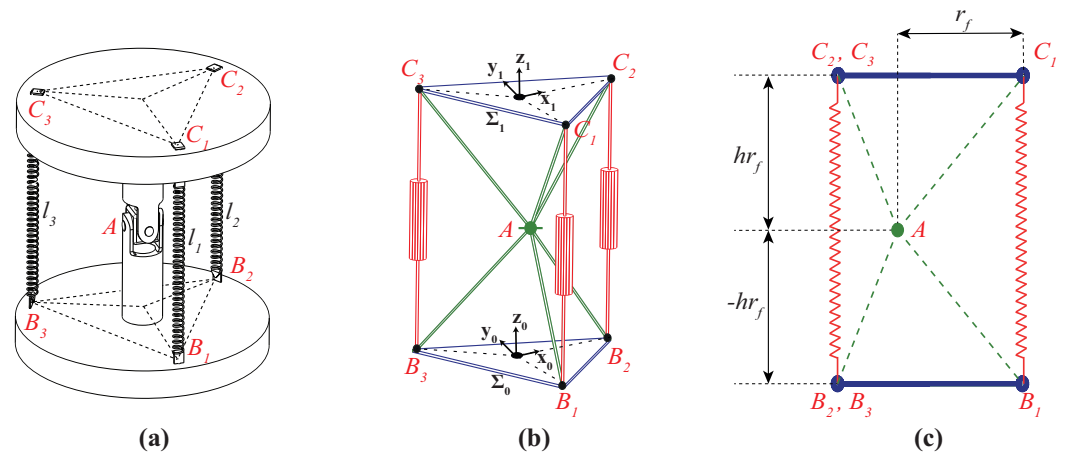


Figure 3. Representation of the (a) parallel mechanism at home pose, (b) 3D view of the correlation to a 3-SPS-U manipulator and (c) 2D view of the manipulator.

Equation (1) provides the coordinates of B_i in the fixed coordinate frame Σ_0 . To determine the position of the end-effector, the Euler angles are usually employed [15], especially to study the singular configurations. In this case, the T&T angles are revisited from [17] for identifying singular configurations. It must be noted that in [17], the singularity analysis was not performed for the T&T space. As the torsion for the mechanism has been constrained, the tilt and azimuth angles are sufficient to analyze the architecture. The representation of the tilt and azimuth angles on the mechanism is revisited from [17] and it is shown below in Figure 4.

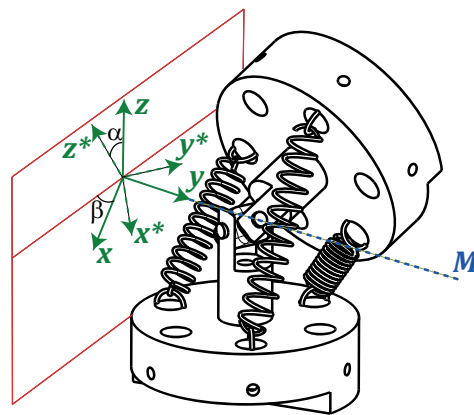


Figure 4. Representation of the tilt (α) and azimuth (β) angles on the parallel mechanism under study.

This representation is correlated with the study shown by Bonev et al. [3], where β represents the azimuth angle between the x -axis and the face of z -axis. A rotation about M causes a shift of the axis xyz to $x^*y^*z^*$. The angle between z and z^* represents the tilt angle, α . Here, the resultant rotation matrix \mathbf{R} is a modified form of the equation presented in [3] by Bonev et al. but in this case without the torsion. The matrix is given by the equation:

$$\mathbf{R} = \mathbf{R}_z(\beta)\mathbf{R}_x(\alpha)\mathbf{R}_z(-\beta) \tag{2}$$

$$\mathbf{R} = \begin{bmatrix} \cos(\beta)^2 + \sin(\beta)^2 \cos(\alpha) & \cos(\beta) \sin(\beta)(1 - \cos(\alpha)) & \sin(\beta) \sin(\alpha) \\ \cos(\beta) \sin(\beta)(1 - \cos(\alpha)) & \sin(\beta)^2 + \cos(\beta)^2 \cos(\alpha) & -\cos(\beta) \sin(\alpha) \\ -\sin(\beta) \sin(\alpha) & \cos(\beta) \sin(\alpha) & \cos(\alpha) \end{bmatrix} \tag{3}$$

$$\text{where } \mathbf{R}_x(\alpha) = \begin{bmatrix} 1 & 0 & 0 \\ 0 & \cos(\alpha) & -\sin(\alpha) \\ 0 & \sin(\alpha) & \cos(\alpha) \end{bmatrix}, \mathbf{R}_z(-\beta) = \begin{bmatrix} \cos(\beta) & \sin(\beta) & 0 \\ -\sin(\beta) & \cos(\beta) & 0 \\ 0 & 0 & 1 \end{bmatrix}.$$

The moving coordinate frame of the end-effector is represented by Σ_1 . The spring mounting points of the end-effector are represented by C_1, C_2 and C_3 for the mechanism. In order to obtain the position of the end-effector, Equation (2) is multiplied by the vector coordinates of C_i , which are given by:

$$\mathbf{c}_i^1 = \mathbf{R} \mathbf{o}_i^1, \text{ with } i = 1, 2, 3 \ \& \ \mathbf{o}_i^1 = \begin{bmatrix} r_f \cos\left(\frac{2\pi(i-1)}{3}\right) \\ r_f \sin\left(\frac{2\pi(i-1)}{3}\right) \\ r_f h \end{bmatrix} \tag{4}$$

In Equation (4), \mathbf{o}_i^1 are the coordinates of C_i in the mobile reference frame Σ_1 of the end-effector. The length of the mechanism l_i , which provides the solution for the inverse kinematic problem (IKP), can be solved by computing the distance between the vector coordinates of the base and the end-effector. The constraint equations are given by:

$$\|\mathbf{b}_i^0 - \mathbf{c}_i^1\| = l_i \text{ where } \mathbf{b}_i^0 = [b_{ix}, b_{iy}, b_{iz}]^T, \mathbf{c}_i^1 = [c_{ix}, c_{iy}, c_{iz}]^T \text{ with } i = 1, 2, 3 \tag{5}$$

$$2 r_f^2 \left((\cos(\beta))^2 \cos(\alpha) - 2 \sin(\beta) \sin(\alpha) h + \cos(\alpha) h^2 - (\cos(\beta))^2 + h^2 - \cos(\alpha) + 1 \right) = l_1^2 \tag{6a}$$

$$-0.5 r_f^2 (2 \cos(\beta) \sin(\beta) \cos(\alpha) \sqrt{3} - 4 \sqrt{3} \cos(\beta) \sin(\alpha) h + 2 (\cos(\beta))^2 \cos(\alpha) - 2 \cos(\beta) \sin(\beta) \sqrt{3} - 4 \sin(\beta) \sin(\alpha) h - 4 h^2 \cos(\alpha) - 2 (\cos(\beta))^2 - 4 h^2 + \cos(\alpha) - 1) = l_2^2 \tag{6b}$$

$$-0.5 r_f^2 (-2 \cos(\beta) \sin(\beta) \cos(\alpha) \sqrt{3} + 4 \sqrt{3} \cos(\beta) \sin(\alpha) h + 2 (\cos(\beta))^2 \cos(\alpha) + 2 \cos(\beta) \sin(\beta) \sqrt{3} - 4 \sin(\beta) \sin(\alpha) h - 4 h^2 \cos(\alpha) - 2 (\cos(\beta))^2 - 4 h^2 + \cos(\alpha) - 1) = l_3^2 \tag{6c}$$

Equations (6a)–(6c) represents the solutions to the IKP. For known values of the tilt and azimuth angles as well as the design parameters r_f and h , these equations can be employed to calculate the distance between the base and end-effector of the mechanism.

3. Singularity Analysis and Workspace of the Mechanism in the T&T Space

This section focuses on the singularity analysis of the mechanism. With the presence of the universal joint, the end-effector coordinates are identified conventionally using the Euler XY rotation angles about the origin A shown in Figure 3. In this approach, for each position of the end-effector, the influence of both rotation angles must be taken into account. However, with the help of the tilt and azimuth angles, it is still possible to analyze the presence of singularities in the mechanism. Moreover, in the T&T space, the mechanism will be simpler to analyze wherein one of the angles remains fixed or constant while the other changes. In [17], only the analysis of joint limits was carried out by setting minimum and maximum values for each prismatic link. This analysis provided the tilt angles for the joint limits; however, the direct kinematic problem (DKP), which presents the singularity-free workspace in T&T space, was not solved in [17]. The singularity-free workspace is thus identified by analyzing the mechanism in the T&T space, which provides the solution to the DKP and the tilt limits.

3.1. Singularity Equations of the Mechanism

For a parallel mechanism, the singularity equation is given by the well-known equation [20]:

$$\mathbf{A}\mathbf{t} + \mathbf{B}\dot{\rho} = 0 \tag{7}$$

where \mathbf{t} represents the angular velocity vector

and $\dot{\rho} = [\dot{l}_1, \dot{l}_2, \dot{l}_3]^T$ represents the joint velocity vector

The IKP Equations (6a)–(6c) are employed in Equation (7), where their time derivatives are taken to study the singularities. In Equation (7), \mathbf{A} represents the direct-kinematics matrix or forward Jacobian matrix and \mathbf{B} represents the inverse-kinematics matrix or inverse Jacobian matrix of the mechanism. The pose variables for the mechanism are the tilt and azimuth angles α and β . The articular variables are the lengths: l_1, l_2 and l_3 . A parallel mechanism in general might encounter three types of singularities, namely, Type-1, Type-2 and Type-3 [21,22]. When the determinant of the direct kinematics matrix \mathbf{A} loses its rank, the determinant of this matrix becomes zero and this scenario leads to parallel singularities or Type-2 singularities. From the number of pose variables and articular variables, it could be seen that matrix \mathbf{A} does not correspond to an $n \times n$ square matrix. For identifying the singularity equations and to construct a square matrix, the 3-SPS-U mechanism is split into three sets of 2-SPS-U architecture, which comprise the length pairs $l_1 - l_2, l_2 - l_3$ and $l_1 - l_3$. The corresponding direct kinematic matrices \mathbf{A} are created for the three sets by differentiating Equations (6a)–(6c) with respect to the pose variables. The matrices are given by:

$$\mathbf{A}_{1-2} = \begin{bmatrix} \frac{\partial L_1}{\partial \alpha} & \frac{\partial L_1}{\partial \beta} \\ \frac{\partial L_2}{\partial \alpha} & \frac{\partial L_2}{\partial \beta} \end{bmatrix}, \mathbf{A}_{2-3} = \begin{bmatrix} \frac{\partial L_2}{\partial \alpha} & \frac{\partial L_2}{\partial \beta} \\ \frac{\partial L_3}{\partial \alpha} & \frac{\partial L_3}{\partial \beta} \end{bmatrix}, \mathbf{A}_{1-3} = \begin{bmatrix} \frac{\partial L_1}{\partial \alpha} & \frac{\partial L_1}{\partial \beta} \\ \frac{\partial L_3}{\partial \alpha} & \frac{\partial L_3}{\partial \beta} \end{bmatrix} \tag{8}$$

In Equation (8), L_1, L_2 and L_3 represent the left-hand sides of Equations (6a)–(6c). The parallel singularities are analyzed by calculating the determinant of matrices in Equation (8) and equating them to zero. The determinant values are given by:

$$\begin{aligned} \det(\mathbf{A}_{1-2}), \mathcal{D}_{p1} : & -4 \sin(\beta)(\cos(\alpha))^2(\cos(\beta))^2\sqrt{3}h + 2 \sin(\beta)(\cos(\alpha))^2\sqrt{3}h^3 \\ & - 2 \sin(\alpha) \cos(\alpha)(\cos(\beta))^2\sqrt{3}h^2 + 6 \sin(\beta) \sin(\alpha) \cos(\alpha) \cos(\beta)h^2 \\ & + 8 \sin(\beta) \cos(\alpha)(\cos(\beta))^2\sqrt{3}h + 2 \sin(\alpha)(\cos(\beta))^2\sqrt{3}h^2 \\ & - 6 (\cos(\alpha))^2 \cos(\beta)h^3 - 6 \sin(\beta) \sin(\alpha) \cos(\beta)h^2 - 4 \sin(\beta)(\cos(\beta))^2\sqrt{3}h \\ & - 2 \sin(\beta)\sqrt{3}h^3 + \sin(\alpha) \cos(\alpha)(\cos(\beta))^2\sqrt{3} - 3 \sin(\alpha) \cos(\alpha)\sqrt{3}h^2 \\ & - 3 \sin(\beta) \sin(\alpha) \cos(\alpha) \cos(\beta) - 2 \sin(\beta) \cos(\alpha)\sqrt{3}h - \sin(\alpha)(\cos(\beta))^2\sqrt{3} \\ & - \sin(\alpha)\sqrt{3}h^2 + 3 (\cos(\alpha))^2 \cos(\beta)h + 6 \cos(\beta)h^3 + 3 \sin(\beta) \sin(\alpha) \cos(\beta) \\ & + 2 \sin(\beta)\sqrt{3}h - \sin(\alpha) \cos(\alpha)\sqrt{3} + \sin(\alpha)\sqrt{3} - 3 \cos(\beta)h = 0 \end{aligned} \tag{9}$$

$$\begin{aligned} \det(\mathbf{A}_{2-3}), \mathcal{D}_{p2} : & 8 \sin(\beta)(\cos(\alpha))^2(\cos(\beta))^2h + 8 \sin(\beta)(\cos(\alpha))^2h^3 \\ & - 8 (\cos(\beta))^2 \sin(\alpha)h^2 \cos(\alpha) - 16 \sin(\beta) \cos(\alpha)(\cos(\beta))^2h \\ & + 8 \sin(\alpha)(\cos(\beta))^2h^2 - 6 \sin(\beta)(\cos(\alpha))^2h + 8 \sin(\beta)(\cos(\beta))^2h \\ & - 8 \sin(\beta)h^3 + 4 (\cos(\beta))^2 \sin(\alpha) \cos(\alpha) + 12 \cos(\alpha)h^2 \sin(\alpha) \\ & + 4h \sin(\beta) \cos(\alpha) - 4 (\cos(\beta))^2 \sin(\alpha) - 4h^2 \sin(\alpha) + 2 \sin(\beta)h \\ & - \sin(\alpha) \cos(\alpha) + \sin(\alpha) = 0 \end{aligned} \tag{10}$$

$$\begin{aligned}
 \det(\mathbf{A}_{1-3}), \mathcal{D}_{p3} : & 4 \sin(\beta)(\cos(\alpha))^2(\cos(\beta))^2\sqrt{3}h - 2 \sin(\beta)(\cos(\alpha))^2\sqrt{3}h^3 \\
 & + 2 \sin(\alpha) \cos(\alpha)(\cos(\beta))^2\sqrt{3}h^2 + 6 \sin(\beta) \sin(\alpha) \cos(\alpha) \cos(\beta)h^2 \\
 & - 8 \sin(\beta) \cos(\alpha)(\cos(\beta))^2\sqrt{3}h - 2 \sin(\alpha)(\cos(\beta))^2\sqrt{3}h^2 \\
 & - 6 (\cos(\alpha))^2 \cos(\beta)h^3 - 6 \sin(\beta) \sin(\alpha) \cos(\beta)h^2 + 4 \sin(\beta)(\cos(\beta))^2\sqrt{3}h \\
 & + 2 \sin(\beta)\sqrt{3}h^3 - \sin(\alpha) \cos(\alpha)(\cos(\beta))^2\sqrt{3} + 3 \sin(\alpha) \cos(\alpha)\sqrt{3}h^2 \\
 & - 3 \sin(\beta) \sin(\alpha) \cos(\alpha) \cos(\beta) + 2 \sin(\beta) \cos(\alpha)\sqrt{3}h + \sin(\alpha)(\cos(\beta))^2\sqrt{3} \\
 & + \sin(\alpha)\sqrt{3}h^2 + 3 (\cos(\alpha))^2 \cos(\beta)h + 6 \cos(\beta)h^3 + 3 \sin(\beta) \sin(\alpha) \cos(\beta) \\
 & - 2 \sin(\beta)\sqrt{3}h + \sin(\alpha) \cos(\alpha)\sqrt{3} - \sin(\alpha)\sqrt{3} - 3 \cos(\beta)h = 0
 \end{aligned} \tag{11}$$

Using Equations (10) and (12), it is possible to identify the pose variables and understand the presence of parallel singularities in the mechanism. On the other hand, when the determinant of the inverse kinematics matrix \mathbf{B} loses its rank, the determinant of this matrix becomes zero and this scenario leads to serial singularities or Type-1 singularities. Similar to the parallel singularity equations, the inverse kinematics matrix \mathbf{B} is created by differentiating the right-hand side of Equations (6a)–(6c) with respect to the articular variables. Following this, the determinant of these matrices is computed and equated to zero for verifying the serial singularities. The matrices and the determinant values are given by:

$$\mathbf{B}_{1-2} = \begin{bmatrix} \frac{\partial R_1}{\partial l_1} & \frac{\partial R_1}{\partial l_2} \\ \frac{\partial R_2}{\partial l_1} & \frac{\partial R_2}{\partial l_2} \end{bmatrix}, \mathbf{B}_{2-3} = \begin{bmatrix} \frac{\partial R_2}{\partial l_2} & \frac{\partial R_2}{\partial l_3} \\ \frac{\partial R_3}{\partial l_2} & \frac{\partial R_3}{\partial l_3} \end{bmatrix}, \mathbf{B}_{1-3} = \begin{bmatrix} \frac{\partial R_1}{\partial l_1} & \frac{\partial R_1}{\partial l_3} \\ \frac{\partial R_3}{\partial l_1} & \frac{\partial R_3}{\partial l_3} \end{bmatrix} \tag{12}$$

$$\det(\mathbf{B}_{1-2}), \mathcal{D}_{s1} : l_1l_2 = 0, \det(\mathbf{B}_{2-3}), \mathcal{D}_{s2} : l_2l_3 = 0, \det(\mathbf{B}_{1-3}), \mathcal{D}_{s3} : l_1l_3 = 0 \tag{13}$$

In Equation (12), R_1 , R_2 and R_3 represent the right-hand side of Equations (6a)–(6c). From Equation (13), when the determinant of the inverse kinematics matrices is equated to zero, serial singularities can occur only when the length of one or two prismatic springs becomes zero. This condition is not feasible for the mechanism under study as the prismatic springs cannot have a length of 0 mm. Thus, there exist no serial singularities in the mechanism. The Type-3 singularities exist when a parallel mechanism encounters both serial and parallel singularities. Since there exist no serial singularities in the mechanism, only the parallel singularities Equations (10)–(12) are analyzed to extract the feasible workspace of the mechanism.

3.2. Results of Singularity Analysis Using the CAD Algorithm

In order to extract the tilt limits for the mechanism from the workspace, the SIROPA library of Maple is employed [23]. The vector coordinates of base from Equation (1), the end-effector coordinates from Equation (4) and the inverse kinematics Equations (6a)–(6c) that map the base to the end-effector are used as inputs for the *CreateManipulator* function of the SIROPA library. This function virtually constructs the 3-SPS-U manipulator in Maple [23,24]. The tilt and azimuth angles are set as the pose variables and the lengths (l_1 , l_2 and l_3) are set as the articular variables for computations. Then, using the *ParallelSingularities* function of SIROPA, the Type-2 singularities Equations (10)–(12) are generated. The actual prototype that will be incorporated with the piping-inspection robot has the design parameters r_f as 11 mm and $h = 0.6$ [16]. As an experimental validation is carried out in the upcoming section, a scaled value of $r_f = 56.7$ mm for $h = 0.6$ is chosen for the singularity analysis [25]. As the constraint equations require joint limits for analysis, the minimum and maximum lengths for each prismatic spring are set as $l_{min} = 40$ mm and $l_{max} = 106$ mm. The Cylindrical Algebraic Decomposition (CAD) algorithm is then employed to analyze the workspace of the mechanism. This approach was proposed for parallel robots by Chablat et al. [26] wherein the workspace, as well as the joint space, are decomposed into cells from $\mathcal{C}_1, \dots, \mathcal{C}_k$. The steps involved in this computation are:

- C_k is an open connected subset of the workspace
- for all pose values in C_k , the direct (resp. inverse) kinematics problem has a constant number of solutions
- C_k is maximal in the sense if C_k is contained in a set \mathcal{E} , then \mathcal{E} does not satisfy the first or second condition.

In Maple, the SIROPA library is exploited to use the CAD algorithm for the parallel mechanism [26] and the analysis is carried out as follows:

- Computation of a subset of the workspace (resp. joint space) where the number of solutions changes: the *discriminant variety*
- Description of the complementary of the discriminant variety in connected cells: the *Generic Cylindrical Algebraic Decomposition*
- Connecting the cells that belong to the same connected component of the complementary of the discriminant variety: *interval comparisons*

Discriminant varieties can be computed using basic and well-known tools from computer algebra such as the Groebner bases [27]. A general framework for computing such objects is available through the *RootFinding[Parametric]* function of Maple. For extracting the workspace of the mechanism, the CAD algorithm combined with the parametric root-finding technique of Maple is employed to find solutions to the DKP for the tilt and azimuth angles [28]. This is carried out using the *CellDecompositionPlus* function of the SIROPA library in Maple [23,24]. The parallel singularity Equations (10)–(12) and the joint limit Equations (6a)–(6c) are transformed as inequalities for isolating the aspects around the home pose. The results of the workspace generated by the CAD algorithm for the tilt and azimuth angles are represented in Figure 5. In Figure 5a, the blue regions indicate the feasible workspaces for the mechanism where there exists one solution to the DKP. The white regions are the zones where there exists no solution. Around the home pose, a larger workspace could be observed. Beyond the singularity zones, it is also possible to identify solutions for the direct kinematics problem, especially between $-\pi$ to $-2\pi/3$ and $2\pi/3$ to π radians. However, in order to attain these positions, the mechanism has to cross singularity boundaries, which might lead to locking of the mechanism in singular modes. Thus, the workspace around the home pose is isolated and they are represented in Figure 5b. Based on observations from Figure 5b, the maximum tilt limits that could be attained or reached by the mechanism corresponds to $\pm\pi/6$ radians. These limits are represented by dotted orange lines in Figure 5b. Thus, for a maximum input tilt of $\alpha = \pm\pi/6$ radians, the mechanism is capable of following a circular trajectory around the home pose.

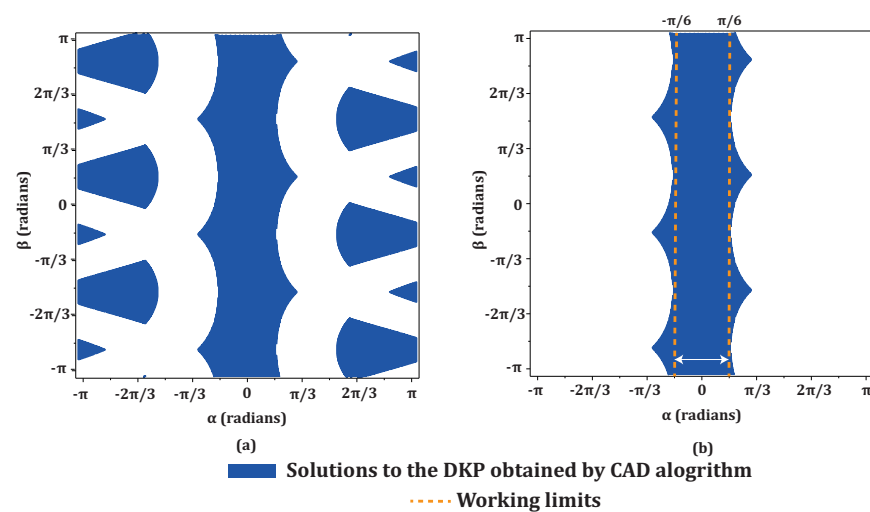


Figure 5. Representation of (a) singularities and workspace zones for the mechanism at $l_{min} = 40$ mm and (b) extraction of feasible workspace around home pose at $l_{min} = 40$ mm.

4. Mapping the T&T Angles to the Euler Angles

The singularity analysis helped in understanding the tilt limits for the 3-SPS-U parallel mechanism using the theory of T&T. However, these results must be mapped with respect to the Euler angles of the universal joint. The 3-SPS-U architecture demonstrated in Figure 3a at the home pose has two degrees of freedom about the universal joint in the center. The conventional approach to identify the vector coordinates of C_i exploits the XY Euler angles about the origin A of the mechanism. In the Euler space, the two angles about the x and y axes are considered as η and ϕ . The transformation matrix \mathbf{E} about the universal joint is given by:

$$\mathbf{E} = \mathbf{R}_x(\eta)\mathbf{R}_y(\phi) = \begin{bmatrix} \cos(\phi) & 0 & \sin(\phi) \\ \sin(\eta)\sin(\phi) & \cos(\eta) & -\sin(\eta)\cos(\phi) \\ -\cos(\eta)\sin(\phi) & \sin(\eta) & \cos(\eta)\cos(\phi) \end{bmatrix} \quad (14)$$

where $\mathbf{R}_x(\eta) = \begin{bmatrix} 1 & 0 & 0 \\ 0 & \cos(\eta) & -\sin(\eta) \\ 0 & \sin(\eta) & \cos(\eta) \end{bmatrix}$, $\mathbf{R}_y(\phi) = \begin{bmatrix} \cos(\phi) & 0 & \sin(\phi) \\ 0 & 1 & 0 \\ -\sin(\phi) & 0 & \cos(\phi) \end{bmatrix}$.

In Equation (14), $\mathbf{E} \in SE(3)$ represents the spatial transformation matrix obtained from the Euler angles of the universal joint. This matrix is used to identify the end-effector coordinates, which are given by:

$$\mathbf{c}_i^1 = \mathbf{E} \mathbf{o}_i^1, \quad \text{with } i = 1, 2, 3 \quad (15)$$

In Equation (15), \mathbf{o}_i^1 are the coordinates of C_i in the mobile reference frame Σ_1 whose vector equation is given in Equation (4). The inverse kinematic model that determines the length of the prismatic springs is computed by calculating the distance between the base and end-effector at the home pose and working conditions. The constraint equations in the Euler space are given by:

$$2r_f^2(\cos(\phi)(h^2 \cos(\eta) - 1) - h \sin(\phi)(\cos(\eta) + 1) + h^2 + 1) = l_1^2 \quad (16a)$$

$$2r_f^2\left(\frac{\sqrt{3}}{2} \sin(\eta) \left(h \cos(\phi) + h + \frac{\sin(\phi)}{2}\right) + \cos(\phi) \left(h^2 \cos(\eta) - \frac{1}{4}\right) + \frac{h \sin(\phi)}{2} (1 + \cos(\eta))\right) + h^2 - \frac{3 \cos(\eta)}{4} + 1 = l_2^2 \quad (16b)$$

$$-2r_f^2\left(\frac{\sqrt{3}}{2} \sin(\eta) \left(h \cos(\phi) + h + \frac{\sin(\phi)}{2}\right) - \cos(\phi) \left(h^2 \cos(\eta) - \frac{1}{4}\right) - \frac{h \sin(\phi)}{2} (1 + \cos(\eta))\right) - h^2 + \frac{3 \cos(\eta)}{4} - 1 = l_3^2 \quad (16c)$$

In the T&T space, the mechanism is initially tilted to its maximum limit, i.e., $\alpha = \pi/6$ radians. Once this limit is reached, α remains a constant, whereas β changes from 0 to 2π radians, thereby achieving a complete revolution in the counter-clockwise direction. In the Euler space, the initial tilt is performed by keeping η as 0 radians and tilting $\phi = \pi/6$ radians. Unlike the T&T space, both the angles are modified as a function of the angle β in the Euler space to achieve a complete revolution. The actuation sequence of the mechanism in both spaces is provided in Table 1. This table demonstrates the relation between the T&T space and the Euler space. For each position of β between 0 to 2π , each and every value of the angles η and ϕ is computed as a function of α and β as demonstrated in Table 1 to achieve the mapping in the Euler space. A simulation of this mapping was performed in MATLAB and the video link is provided at the bottom of this page (Video link for the simulation in MATLAB: Available online: https://drive.google.com/file/d/1xXPY4oU_Q04SgcU1kcQn9qt_9WIT2N5E/view?usp=share_link (accessed on: 15 January 2023) 1× Speed, Available online: https://drive.google.com/file/d/1RrIgmipxXAAhKP71hspWao4t4OM5XT4dL/view?usp=share_link (accessed on 15 January 2023) 0.4× Speed). The postures of the

mechanism in both the spaces at the home pose and working conditions are represented in Figure 6.

Table 1. The actuation angles for the mechanism in the T&T space and the Euler space.

Movement Type	Tilt Space		Euler Space	
	α (Radians)	β (Radians)	η (Radians)	ϕ (Radians)
Initial tilt	$0 \rightarrow \pi/6$	0	0	$0 \rightarrow \pi/6$
Circular path	$\pi/6$	$0 \rightarrow 2\pi$	$\alpha \sin(\beta)$	$\alpha \cos(\beta)$
Return to home	$\pi/6 \rightarrow 0$	0	0	$\pi/6 \rightarrow 0$

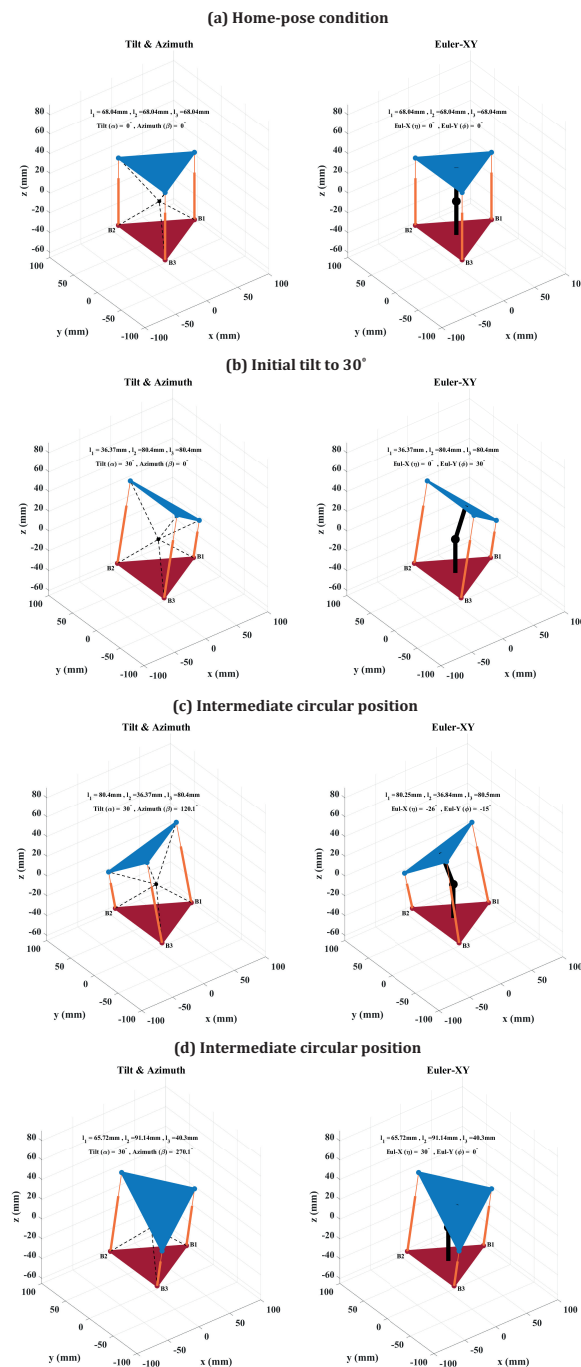


Figure 6. Postures of the 3-SPS-U mechanism in the T&T space and the Euler space.

5. Experimental Validation

In this section, the mapping theory is validated by performing a circular trajectory on the parallel mechanism. The prototype of the 3-SPS-U parallel mechanism is realized at LS2N, France with a universal joint of length 68 mm. As explained earlier, a value of $r_f = 56.7$ mm was considered for $h = 0.6$. The base and end-effector of the mechanism are realized by rapid prototyping. Using tension springs and supports, the base and end-effector are connected. The control of this mechanism is carried out using a BeagleBone (BB) black microcomputer. Three Maxon DC motors coupled with quadrature encoders are employed to tilt the mechanism. In order to have a static model and higher torques, a planetary gearhead with a reduction of 1621:1 is coupled to each DC motor. A 36/2 servo-controller is employed for each motor to control the position. The three DC motors are assembled on a platform, which is made by rapid prototyping. As the distance between the gearbox output shaft and the mechanism was higher, an extended shaft with a flange coupling is employed to connect to the gearbox shaft. A 40 mm diameter pulley is assembled on the extended shaft and a cable of 1.5 mm diameter is wound over this pulley. The other end of the cable connects to the end-effector mounting support by passing through each spring. For eliminating the effects of radial play in the pulley shaft, flange couplings are employed. The cables are assembled in such a way that at the home pose, the tension along the cables is high. The entire experimental setup and its digital model are represented below in Figure 7. The experiments are carried out for two orientations: vertical and horizontal under no-load conditions. The vertical orientation is in line with the orientation of the piping-inspection robot inside a vertical pipeline and this posture is represented in Figure 7a. The horizontal orientation is in-line with the orientation of the robot inside a horizontal pipeline, as shown in Figure 1.

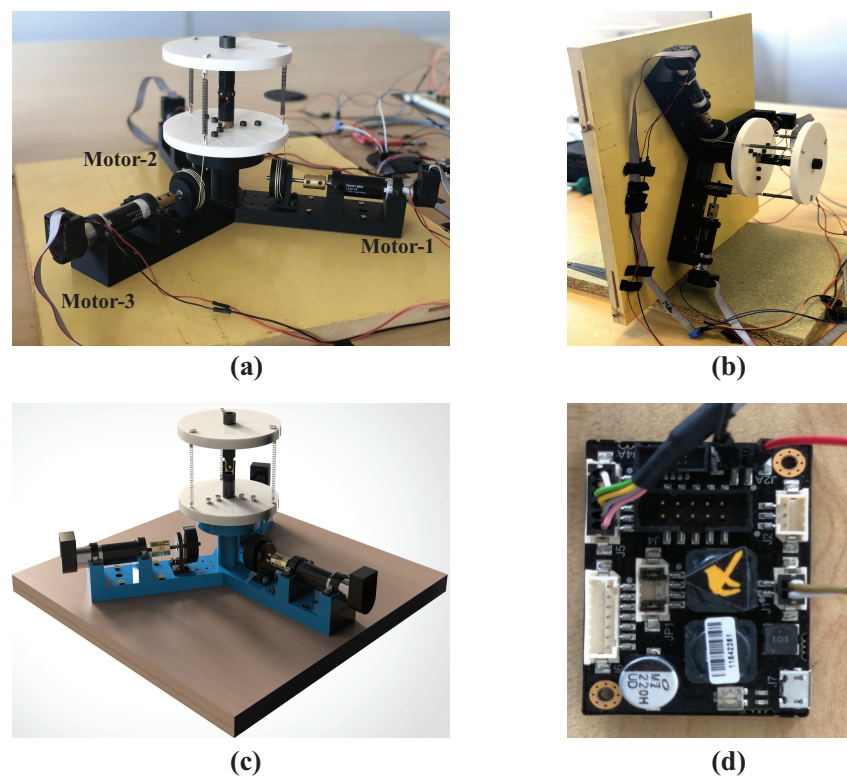


Figure 7. Representation of the (a) experimental setup of the mechanism in vertical orientation, (b) experimental setup of the mechanism in horizontal orientation, (c) digital model of the experimental setup and (d) one of the three ESCON 36/2 servo-controllers.

5.1. Trajectory Generation

For the experiments, at each instance of the control loop, the tilt angles of the Euler space η and ϕ were passed as inputs to solve the IKP. This actuation is carried out through the cables that pass through the springs of the mechanism. The pose variables and the articular variables for the mechanism are given by $\mathbf{q} = [\eta, \phi]$ and $\rho = [l_1, l_2, l_3]$ [25]. The length of the springs is calculated using Equations (16a)–(16c) in the Euler space. The IKP for each spring is converted into angular displacements of the pulley, which will be the target position for each DC motor. The equation for the desired angular position of the pulley with respect to the IKP is given by:

$$\theta_{di} = \frac{(l_i - l_{home})}{r}, \text{ with } i = 1, 2, 3 \tag{17}$$

In Equation (17), θ_{di} is the desired angular position calculated from IKP for given input tilt angles η and ϕ . The parameter r indicates the pulley radius, which is 20 mm. At the home position, the value of l_{home} is 68 mm. For every angular displacement of the DC motor, the encoder data are passed to the BB black ports. The angular displacement of the pulley from the encoder channel information can be calculated by:

$$\theta_{mi} = \frac{E_i \pi}{2CG}, \text{ with } i = 1, 2, 3 \tag{18}$$

In Equation (18), E_i indicates the output data of the encoder channels of Motor- i . The angle θ_{mi} is the measured angular displacement at the output shaft of the gearbox. C indicates the counts per revolution of the encoder, which is 500, and G is the reduction ratio of the gearbox, and these values are taken from the technical datasheet of the encoder and the gearbox unit. At a given tilt angle, the mechanism tries to attain the position θ_{di} . For the trajectory planning, the fifth-degree polynomial equation proposed by Khalil et al. [29] is employed. This equation is used to define the position $s(t)$, velocity $\dot{s}(t)$ and acceleration $\ddot{s}(t)$ for the mechanism and they are given by:

$$s(t) = 10 \left(\frac{t}{t_f} \right)^3 - 15 \left(\frac{t}{t_f} \right)^4 + 6 \left(\frac{t}{t_f} \right)^5 \tag{19}$$

$$\dot{s}(t) = 30 \left(\frac{t^2}{t_f^3} \right) - 60 \left(\frac{t^3}{t_f^4} \right) + 30 \left(\frac{t^4}{t_f^5} \right) \tag{20}$$

$$\ddot{s}(t) = 60 \left(\frac{t}{t_f^3} \right) - 180 \left(\frac{t^2}{t_f^4} \right) + 120 \left(\frac{t^3}{t_f^5} \right) \tag{21}$$

An initial linear tilt is performed for the mechanism before performing the circular trajectory. For the trajectory generation, the simulation time t_f is estimated and it is given by:

$$t_f = \max(\gamma_V, \sqrt{\gamma_A}) \tag{22}$$

In Equation (22), γ_V is the ratio of the maximum joint velocity to the speed of the motor and γ_A is the ratio of the maximum joint acceleration to the acceleration of the motor [8]. In order to demonstrate the circular trajectory, the T&T angles must be mapped to the Euler space in the control law. Using Table 1, the mapping is incorporated in the control law and it is implemented using the equation:

$$\mathbf{D}(t) = \begin{bmatrix} \eta \\ \phi \end{bmatrix} = \begin{bmatrix} \alpha \sin(\beta s(t)) \\ \alpha \cos(\beta s(t)) \end{bmatrix} \tag{23}$$

Equation (23) represents the input tilt angles η and ϕ in the Euler space as a function of the tilt and azimuth angles of the T&T space. α represents the tilt angle and the azimuth value β goes from 0 to 2π radians for a constant tilt to perform a counter-clockwise

circular trajectory in line with the simulation. The corresponding angular velocities and accelerations are given by:

$$\mathbf{V}(t) = \begin{bmatrix} \alpha\beta\dot{s}(t) \cos(\beta s(t)) \\ -\alpha\beta\dot{s}(t) \sin(\beta s(t)) \end{bmatrix} \tag{24}$$

$$\mathbf{A}(t) = \begin{bmatrix} \alpha\beta\ddot{s}(t) \cos(\beta s(t)) - \alpha\beta^2\dot{s}(t)^2 \sin(\beta s(t)) \\ -\alpha\beta\ddot{s}(t) \sin(\beta s(t)) - \alpha\beta^2\dot{s}(t)^2 \cos(\beta s(t)) \end{bmatrix} \tag{25}$$

In order to calculate the Cartesian velocities of the prismatic joints, the Jacobian matrices are employed. The equation is given by:

$$\begin{bmatrix} \dot{l}_1 \\ \dot{l}_2 \\ \dot{l}_3 \end{bmatrix} = \mathbf{J}_c \begin{bmatrix} \dot{\eta} \\ \dot{\phi} \end{bmatrix}, \text{ with } \mathbf{J}_c = \begin{bmatrix} \frac{\partial l_1}{\partial \eta} & \frac{\partial l_1}{\partial \phi} \\ \frac{\partial l_2}{\partial \eta} & \frac{\partial l_2}{\partial \phi} \\ \frac{\partial l_3}{\partial \eta} & \frac{\partial l_3}{\partial \phi} \end{bmatrix} \tag{26}$$

In Equation (26), \mathbf{J}_c represents the direct kinematics matrix (\mathbf{A}). Using Equation (26), the joint velocities are estimated, following which the desired angular velocities of the output shaft can be estimated. The joint coordinate vector can be estimated by the equation:

$$\mathbf{q}(t) = \mathbf{f}(\mathbf{D}(t)) \tag{27}$$

In Equation (27), $\mathbf{f} = [l_1, l_2, l_3]^T$ is the vector that contains the solution of the IKP for the input tilt angles. The joint velocities can be computed with the help of the Jacobian matrix \mathbf{J}_c using the equation:

$$\dot{\mathbf{q}}(t) = \mathbf{J}_c \mathbf{V}(t) \tag{28}$$

The accelerations in the joints can be computed using the Jacobian matrix and its time derivative, whose equation is given by:

$$\ddot{\mathbf{q}}(t) = \dot{\mathbf{J}}_c \mathbf{A}(t) + \mathbf{J}_c \mathbf{V}(t) \tag{29}$$

5.2. PID Control Law

In [10] a force control algorithm was implemented for the control of the piping-inspection robot represented in Figure 1. The same algorithm is employed here for the control of the parallel mechanism. By applying motor torques and current, the mechanism tilts to attain a certain position. Once the desired position is reached, the current and torque are cut off for attaining a static phase. For each angular position of the DC motor, the encoder position data are transmitted to the user by the BB black. However, the output data from the encoders are not directly used to calculate the solutions to the IKP as there exists a significant difference between the desired and measured positions. These differences are caused by factors such as motor inertia, frictional effects and inertial forces. In order to compensate for these factors, a closed-loop PID controller is employed, which tries to minimize the errors between the desired and measured positions. The PID control scheme as provided in [8,30] for calculating the motor torques is given by:

$$\Gamma = J \left(\ddot{\theta}_{di} + K_P(\theta_{di} - \theta_{mi}) + K_D(\dot{\theta}_{di} - \dot{\theta}_{mi}) + K_I \int_0^t (\theta_{di} - \theta_{mi}) \right), \text{ with } i = 1, 2, 3 \tag{30}$$

where θ_{di} , θ_{mi} are the desired and measured positions, $\dot{\theta}_{di}$, $\dot{\theta}_{mi}$ are the desired and measured velocities, $\ddot{\theta}_{di}$ is the desired acceleration.

In Equation (30), Γ represents the output torque at the gearbox after PID correction. From the technical datasheet of the gearbox unit, the inertia J is taken as 4.1×10^{-7} kg·m². The desired positions are computed using the mapping Equation (23) and the IKP relations. The desired velocity and acceleration of each joint is computed with the help of Equations (28) and (29). The measured positions are computed using Equation (18).

In Equation (30), K_P is the proportionality term, which examines the error term and responds proportionally. The integral term K_I tries to reduce the error at each time instant. The overshoot of value from the desired position is compensated by the difference term K_D . Thus, the PID in general takes into account the past step, the present step and the future step such that the error is reduced [31]. The values for the PID terms of Equation (30) are given by:

$$\omega = \frac{k_t k_e}{R J} = 14 \text{ rad/s}$$

$$K_P = 3\omega^2 = 588, K_D = 3\omega = 42, K_I = \omega^3 = 2744 \quad (31)$$

In Equation (31), ω is a parameter that is a function of the torque constant (k_t), the speed constant (k_e), the motor resistance (R) and its inertia (J). It helps to determine the PID parameters K_P , K_D and K_I [32] as per the relation given in Equation (31). This approach was tested and validated on PID control of other robots at LS2N [8,33]. The closed-loop system that is incorporated for the control of the 3-SPS-U mechanism is represented below in Figure 8.

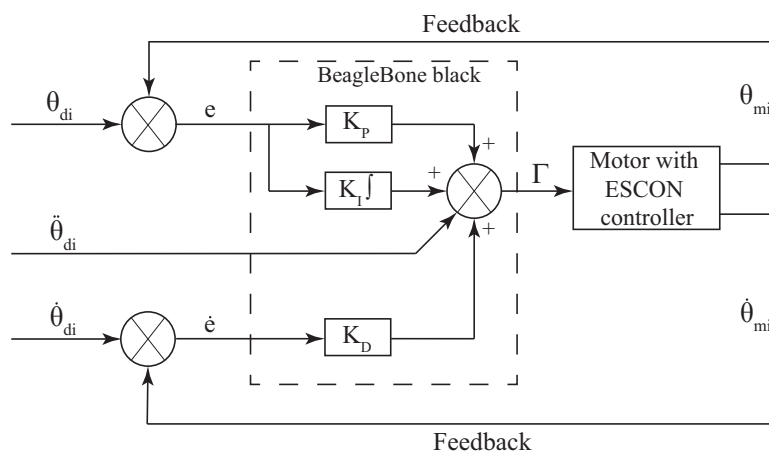


Figure 8. Closed-loop PID controller employed for the mechanism [8].

In Figure 8, e and \dot{e} indicate the error and its derivative, which are computed based on the difference between the desired and measured data. Before the start of experiments, the servo-controllers are calibrated in a computer. The saturation current is used as a reference for controlling the direction of rotation of the DC motors. For safer operations, 90% and 10% duty cycles are set as the limits for the rotation of motors in either direction. The PWM calibration of each servo-controller is carried out as per Table 2. The force control algorithm is executed in the C language using the BB black microcomputer. The link for the algorithm is provided at the bottom of this page (GitHub link for the algorithm: Available online: <https://github.com/stvt1991/Control-of-3-SPS-U-Tensegrity-mechanism> (accessed on 20 January 2023)).

Table 2. ESCON controller calibration for the force control algorithm.

PWM Duty	Nominal Current (A)	Motor Torque (mN·m)	Motor Speed (rpm)
10%	-0.177	-6.05	3720 (Counter-clockwise)
50% (idle)	0	0	0
90%	0.177	6.05	3720 (Clockwise)

5.3. Results of Experiments

For performing the circular trajectory, it is necessary to define the tilt angle α from the T&T space. An initial tilt along one of the motors (Motor-1) is performed. A circular path

in a counter-clockwise direction is then traced by the mechanism. At the end of the circular trajectory, the mechanism is pulled back to its home pose. For the circular trajectory, a tilt of $\alpha = \pi/10$ radians within the workspace of the mechanism is chosen. The circular trajectory experiment is performed in the following sequence:

Home → Motor-1: linear tilt → Circular path (counter-clockwise) → Home: linear tilt

The linear tilt is performed before and after the circular trajectory for a period of 9 s. The circular path is performed for 35 s. Owing to the sleep routines in the control loop, the time taken to initiate the circular trajectory after the initial linear tilt is longer. The total time to perform the experiments is around 124 s. The plot of the joint positions at each instance of the experiments is represented in Figure 9 for both orientations of the mechanism. The initial linear tilt is performed from 0 to $\pi/10$ radians. The circular trajectory is created from this tilt position in the counter-clockwise direction. During the experimental cycle, the prismatic springs extended to a maximum length of 84.7 mm from the home position. The intermediate change in prismatic lengths can be observed in Figure 9a–f between 50 and 100 s for both orientations of the mechanism. The springs connected to each motor also reached a minimum length of 50 mm at $\pi/10$ radians. The zones between 75.9 and 84.6 mm describe the redundancy of the mechanism where one of the springs has limited effects in tilting the mechanism. The error between the measured and desired data can be calculated using the equation:

$$Error = \frac{(\theta_{mi} - \theta_{di})180}{\pi} \quad (32)$$

The plots of the error for both orientations of the mechanism are shown in Figure 10. Due to the frequency issues with the micro-computer, noise could be observed in the final plot. From Figure 10, the error data were found to be between -0.022° and 0.036° in the vertical orientation and between -0.025° and 0.025° in the horizontal orientation. These values were found to be closer to 0, thanks to the calibration of the PID parameters. Similarly, using the current flow data from the algorithm, the output torques were calculated using the motor torque constant. The plots of the motor torques in both orientations are shown in Figure 11. The torque values were between -0.0059 N·m and 0.0053 N·m in the vertical orientation and between -0.0057 N·m and 0.0058 in the horizontal orientation. It could be observed that these values were similar in both orientations. This is due to the fact that the self-weight of the parallel mechanism had a negligible influence on the motor torques, especially for the horizontal configuration. However, with the presence of external loading, the operating torques might vary significantly in both orientations. From Figure 11 it can also be observed that the operating torques were well within the nominal torque rating of the DC motor. A video link that demonstrates the generation of the circular trajectory in the Euler space of the mechanism is provided at the bottom of this page (Video link for the circular trajectory experiments: Available online: <https://uncloud.univ-nantes.fr/index.php/s/b96nfCRTcBESzGo> (accessed on 20 January 2023).

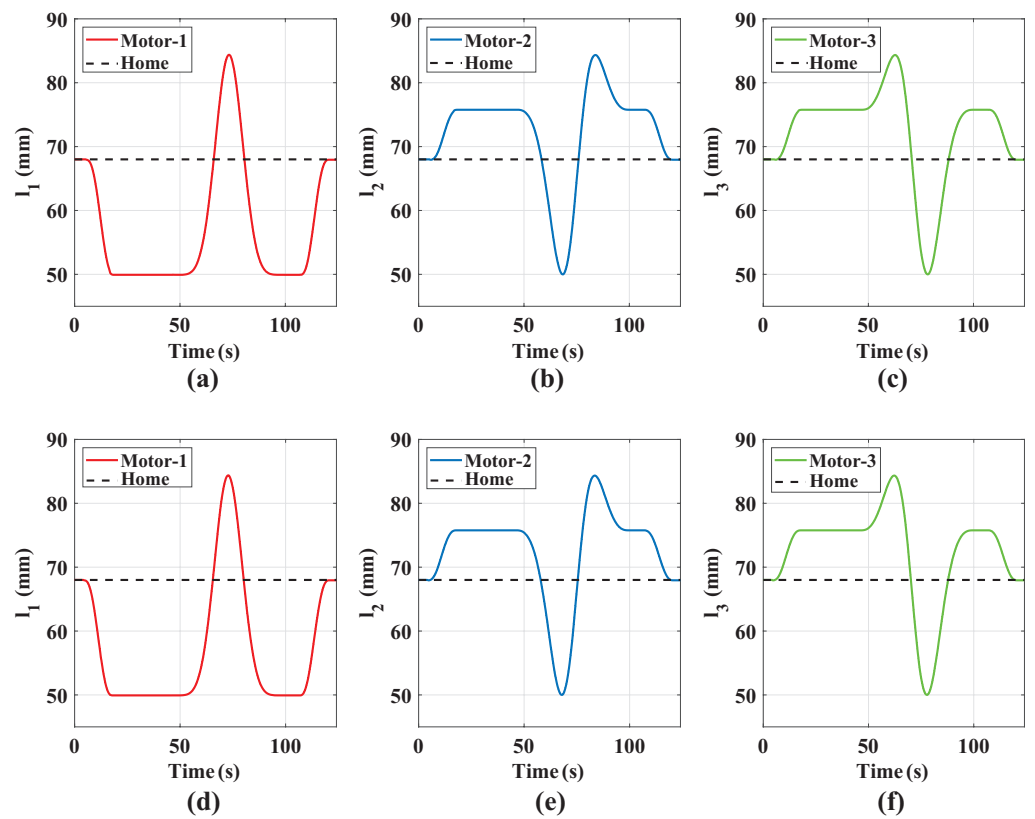


Figure 9. Position of prismatic springs along the circular trajectory in the (a–c): vertical and (d–f): horizontal orientations of the mechanism.

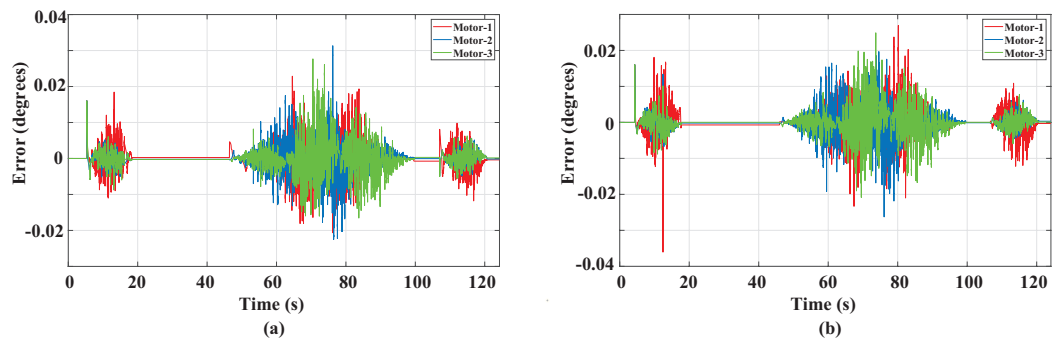


Figure 10. Joint position errors for the (a) vertical and (b) horizontal orientations of the mechanism.

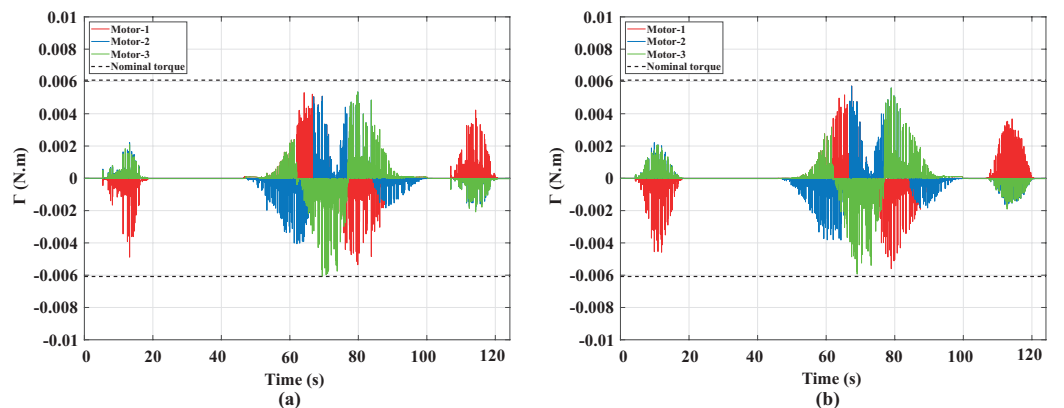


Figure 11. Motor torques generated on each motor during operation in (a) vertical and (b) horizontal orientations of the mechanism.

6. Discussion and Perspectives

This article presented the application of the theory of Tilt and Torsion (T&T) to a spherical parallel mechanism. The estimation of the vector coordinates as well as the inverse kinematics problem is solved conventionally using the Euler angles of the universal joint. However, the singularity approach using these angles will require the analysis of the workspace by considering the presence of both tilt angles, i.e., η and ϕ [15]. This computation was time-consuming and it will be even more complicated to study the workspaces of the mechanism when a stacked model is analyzed as there will be four tilt angles. In order to overcome this issue, the T&T space was considered in this study. The advantage of this method is that for a constant tilt angle, the azimuth can vary between 0 and 2π radians or vice versa. The computation was much simpler and consumes less time through this approach when compared to the Euler space. The mapping was successfully implemented from the T&T space to the Euler space. The numerical simulations were first validated for mapping using MATLAB. Following this, experiments were performed on the prototype of the mechanism. The T&T space was mapped to the Euler space by using the mapping equations and the mechanism was made to perform a counter-clockwise circular trajectory in line with the simulations. At each instance of the trajectory, the equivalent $X - Y$ Euler angles were mapped from the T&T space. The experiments also helped in calculating the error data as well as the torque generated on each motor. It was found that the operating torques were well within the nominal rating of the motor units employed. Since this parallel mechanism is proposed to be implemented in the piping-inspection robot that was presented in Figure 1, the circular trajectory can prove vital to align the axis of the robot assembly with the axis of the pipeline, especially when the robot encounters a pipe bend or a junction. This alignment can be performed using control systems that incorporate the mapping equations and thereby perform a circular path according to the profile of the pipe bend to ensure alignment.

The application of this mapping is proposed to be extended to the study of a two-stage (stacked) model of the 3-SPS-U mechanism. The tilt limits generated by the single stage were around $\pm\pi/6$ radians. These limits were not sufficient to assist the piping-inspection robot to overcome a bend or a junction. With a stacked model, higher tilt limits could be obtained. The singularity analysis of the stacked structure in the Euler space will be computationally expensive due to the presence of four tilt angles. The T&T space will thus be employed and it will lead to the analysis of singularities with two tilt angles and a common azimuth. Moreover, the T&T equations facilitate an easier computational approach to calculate the value of the applied forces on the cables of the mechanism, as demonstrated in [17]. This will be very useful for the prototyping and control strategy of the stacked model in the future. Advanced industrial controllers such as the EtherCAT are proposed to be employed for the control strategy of the mechanism, as the existing BB black micro-computer has some frequency issues. This controller will also help provide an easy interfacing with the piping-inspection robot as well as the parallel mechanism and all these modules could be controlled from a central unit.

Author Contributions: Conceptualization, S.V. and D.C.; methodology, S.V.; numerical simulation, S.V.; experimental validation, S.V. and D.C.; investigation, S.V. and D.C.; writing—original draft presentation, S.V. and D.C.; writing—review and editing, S.V. and D.C. All authors have read and agreed to the published version of the manuscript.

Funding: This work has been funded by the CNRS through the “RobotVer” project within the framework of the project titled PEPS—“Ingénierie Inspirée par la Nature”.

Data Availability Statement: Not applicable.

Acknowledgments: We would like to thank Stéphane Jolivet, Philippe Lemoine and Denis Creusot from LS2N for their extended support in the prototyping of the mechanism and the design of the circuit for the control part.

Conflicts of Interest: The authors declare no conflict of interest.

Abbreviations

The following abbreviations are used in this manuscript:

PKM	Parallel Kinematic Mechanism
T&T	Tilt and Torsion
IKP	Inverse Kinematics Problem
DKP	Direct Kinematics Problem
BB Black	BeagleBone Black

Nomenclature

\mathbf{b}_i	Vector coordinates for base B_i
\mathbf{c}_i	Vector coordinates of mobile platform C_i
r_f	Distance of spring mounting point in mm
h	Design constant of the mechanism (no unit)
\mathbf{R}	Tilt and Azimuth transformation matrix
l_i	Length of i th prismatic spring
α	Tilt angle in T&T space
β	Azimuth angle in T&T space
\mathbf{A}	Direct kinematics matrix
\mathbf{B}	Inverse kinematics matrix
\mathcal{D}	Determinant value of the direct kinematics matrix
\mathbf{E}	Euler angle transformation matrix
η, ϕ	XY tilt/rotation angles in the Euler space
θ_{di}, θ_{mi}	Desired and measured angular positions in rad
$\dot{\theta}_{di}, \dot{\theta}_{mi}$	Desired and measured angular velocities in rad/s
$\ddot{\theta}_{di}$	Desired angular acceleration in rad/s ²
ω	Pulsation in rad/s

References

- Merlet, J.P. *Parallel Robots*; Springer Science & Business Media: Berlin/Heidelberg, Germany, 2006; Volume 128.
- Pritschow, G. Parallel kinematic machines (PKM)—limitations and new solutions. *CIRP Ann.* **2000**, *49*, 275–280. [[CrossRef](#)]
- Bonev, I.A.; Zlatanov, D.; Gosselin, C.M. Advantages of the modified Euler angles in the design and control of PKMs. In Proceedings of the 2002 Parallel Kinematic Machines International Conference, Chemnitz, Germany, 23–25 April 2002; pp. 171–188.
- Bonev, I.A. *Geometric Analysis of Parallel Mechanisms*; Université Laval: Quebec City, QC, Canada, 2002.
- Bonev, I.A.; Ryu, J. Orientation workspace analysis of 6-DOF parallel manipulators. In Proceedings of the International Design Engineering Technical Conferences and Computers and Information in Engineering Conference, Las Vegas, NV, USA, 12–16 September 1999; American Society of Mechanical Engineers: New York City, NY, USA, 1999; Volume 19715, pp. 281–288.
- Briot, S.; Bonev, I.A. Singularity analysis of zero-torsion parallel mechanisms. In Proceedings of the 2008 IEEE/RSJ International Conference on Intelligent Robots and Systems, Nice, France, 22–26 September 2008; IEEE: Piscataway, NJ, USA, 2008; pp. 1952–1957.
- Tao, Z.; An, Q. Interference analysis and workspace optimization of 3-RRR spherical parallel mechanism. *Mech. Mach. Theory* **2013**, *69*, 62–72. [[CrossRef](#)]
- Caro, S.; Chablat, D.; Lemoine, P.; Wenger, P. Kinematic analysis and trajectory planning of the Orthoglide 5-axis. In Proceedings of the International Design Engineering Technical Conferences and Computers and Information in Engineering Conference, Boston, MA, USA, 2–5 August 2015; American Society of Mechanical Engineers: New York City, NY, USA, 2015; Volume 57144, p. V05CT08A004.
- Yang, G.; Teo, T.J.; Chen, I.M.; Lin, W. Analysis and design of a 3-DOF flexure-based zero-torsion parallel manipulator for nano-alignment applications. In Proceedings of the 2011 IEEE International Conference on Robotics and Automation, Shanghai, China, 9–13 May 2011; IEEE: Piscataway, NJ, USA, 2011; pp. 2751–2756.
- Venkateswaran, S.; Chablat, D.; Boyer, F. Numerical and experimental validation of the prototype of a bio-inspired piping inspection robot. *Robotics* **2019**, *8*, 32. [[CrossRef](#)]
- Zhang, Y.; Zhang, M.; Sun, H.; Jia, Q. Design and motion analysis of a flexible squirm pipe robot. In Proceedings of the 2010 International Conference on Intelligent System Design and Engineering Application, Changsha, China, 13–14 October 2010; IEEE: Piscataway, NJ, USA, 2010; Volume 1, pp. 527–531.
- Kwon, Y.S.; Lim, H.; Jung, E.J.; Yi, B.J. Design and motion planning of a two-moduled indoor pipeline inspection robot. In Proceedings of the 2008 IEEE International Conference on Robotics and Automation, Pasadena, CA, USA, 19–23 May 2008; IEEE: Piscataway, NJ, USA, 2008; pp. 3998–4004.

13. Ryew, S.; Baik, S.H.; Ryu, S.W.; Jung, K.M.; Roh, S.G.; Choi, H.R. In-pipe inspection robot system with active steering mechanism. In Proceedings of the 2000 IEEE/RSJ International Conference on Intelligent Robots and Systems (IROS 2000) (Cat. No. 00CH37113), Takamatsu, Japan, 31 October 2000–5 November 2000; IEEE: Piscataway, NJ, USA, 2000; Volume 3, pp. 1652–1657.
14. Venkateswaran, S.; Chablat, D. A new inspection robot for pipelines with bends and junctions. In *Advances in Mechanism and Machine Science, Proceedings of the 15th IFToMM World Congress on Mechanism and Machine Science, Krakow, Poland, 30 June–4 July 2019*; Springer International Publishing: Cham, Switzerland, 2019; pp. 33–42.
15. Venkateswaran, S.; Chablat, D. Singularity and Workspace Analysis of 3-SPSU and 4-SPSU Tensegrity Mechanisms. In *Advances in Robot Kinematics 2020*; Springer International Publishing: Cham, Switzerland, 2021; pp. 226–233.
16. Venkateswaran, S.; Chablat, D.; Hamon, P. An optimal design of a flexible piping inspection robot. *J. Mech. Robot.* **2021**, *13*, 035002. [[CrossRef](#)]
17. Venkateswaran, S.; Furet, M.; Chablat, D.; Wenger, P. Design and analysis of a tensegrity mechanism for a bio-inspired robot. In Proceedings of the International Design Engineering Technical Conferences and Computers and Information in Engineering Conference, Anaheim, CA, USA, 18–21 August 2019; American Society of Mechanical Engineers: New York City, NY, USA, 2019; Volume 59230, p. V05AT07A026.
18. Yigit, C.B.; Boyraz, P. Design and modelling of a cable-driven parallel-series hybrid variable stiffness joint mechanism for robotics. *Mech. Sci.* **2017**, *8*, 65–77. [[CrossRef](#)]
19. Alici, G.; Shirinzadeh, B. Topology optimisation and singularity analysis of a 3-SPS parallel manipulator with a passive constraining spherical joint. *Mech. Mach. Theory* **2004**, *39*, 215–235. [[CrossRef](#)]
20. Gosselin, C.; Angeles, J. Singularity analysis of closed-loop kinematic chains. *IEEE Trans. Robot. Autom.* **1990**, *6*, 281–290. [[CrossRef](#)]
21. Wenger, P.; Chablat, D. Definition sets for the direct kinematics of parallel manipulators. In Proceedings of the 1997 8th International Conference on Advanced Robotics, ICAR'97, Monterey, CA, USA, 7–9 July 1997; IEEE: Piscataway, NJ, USA, 1997; pp. 859–864.
22. Chablat, D.; Wenger, P. Working modes and aspects in fully parallel manipulators. In Proceedings of the 1998 IEEE International Conference on Robotics and Automation (Cat. No. 98CH36146), Leuven, Belgium, 20–20 May 1998; IEEE: Piscataway, NJ, USA, 1998; Volume 3, pp. 1964–1969.
23. Jha, R.; Chablat, D.; Baron, L.; Rouillier, F.; Moroz, G. Workspace, joint space and singularities of a family of delta-like robot. *Mech. Mach. Theory* **2018**, *127*, 73–95. [[CrossRef](#)]
24. Chablat, D.; Moroz, G.; Rouillier, F.; Wenger, P. Using Maple to analyse parallel robots. In *Maple in Mathematics Education and Research, Proceedings of the Third Maple Conference, MC 2019, Waterloo, ON, Canada, 15–17 October 2019*; Proceedings 3; Springer International Publishing: Cham, Switzerland, 2020; pp. 50–64.
25. Venkateswaran, S.; Chablat, D. Trajectory Planning for a 3-SPS-U Tensegrity Mechanism. In Proceedings of the International Design Engineering Technical Conferences and Computers and Information in Engineering Conference, Virtual, 17–20 August 2021; American Society of Mechanical Engineers: New York City, NY, USA, 2021; Volume 85451, p. V08BT08A004.
26. Chablat, D.; Moroz, G.; Wenger, P. Uniqueness domains and non singular assembly mode changing trajectories. In Proceedings of the 2011 IEEE International Conference on Robotics and Automation, Shanghai, China, 9–13 May 2011; IEEE: Piscataway, NJ, USA, 2011; pp. 3946–3951.
27. Cox, D.; Little, J.; OShea, D. *Ideals, Varieties, and Algorithms: An Introduction to Computational Algebraic Geometry and Commutative Algebra*; Springer Science & Business Media: Berlin/Heidelberg, Germany, 2013.
28. Chablat, D.; Ottaviano, E.; Moroz, G. A comparative study of 4-cable planar manipulators based on cylindrical algebraic decomposition. In Proceedings of the International Design Engineering Technical Conferences and Computers and Information in Engineering Conference, Washington, DC, USA, 28–31 August 2011; Volume 54839, pp. 1253–1262.
29. Khalil, W.; Dombre, E. *Modeling Identification and Control of Robots*; CRC Press: Boca Raton, FL, USA, 2002.
30. Jha, R.; Chablat, D.; Rouillier, F.; Moroz, G. Influence of the trajectory planning on the accuracy of the orthoglide 5-axis. In Proceedings of the International Design Engineering Technical Conferences and Computers and Information in Engineering Conference, Charlotte, NC, USA, 21–24 August 2016; American Society of Mechanical Engineers: New York City, NY, USA, 2016; Volume 50152, p. V05AT07A039.
31. Maung, M.M.; Latt, M.M.; Nwe, C.M. DC motor angular position control using PID controller with friction compensation. *Int. J. Sci. Res. Publ.* **2018**, *8*, 149. [[CrossRef](#)]
32. Lemoine, P. *Commande d'un Moteur électrique à Courant Continu Mettant en Mouvement une Charge Inertielle*; Technical Lab Report; Le Laboratoire des Sciences du Numérique de Nantes (LS2N): Nantes, France, 2019.
33. Fasquelle, B.; Furet, M.; Khanna, P.; Chablat, D.; Chevallereau, C.; Wenger, P. A bio-inspired 3-DOF light-weight manipulator with tensegrity X-joints. In Proceedings of the 2020 IEEE International Conference on Robotics and Automation (ICRA), Paris, France, 31 May 2020–31 August 2020; IEEE: Piscataway, NJ, USA, 2020; pp. 5054–5060.

Disclaimer/Publisher's Note: The statements, opinions and data contained in all publications are solely those of the individual author(s) and contributor(s) and not of MDPI and/or the editor(s). MDPI and/or the editor(s) disclaim responsibility for any injury to people or property resulting from any ideas, methods, instructions or products referred to in the content.